

## Controllable Simultaneous Bifacial Cu-Plating for High-Efficiency Crystalline Silicon Solar Cells

Han, Can; Yang, Guangtao; Procel, Paul; O'Connor, Daragh; Zhao, Yifeng; Gopalakrishnan, Anirudh; Zhang, Xiaodan; Zeman, Miro; Mazzarella, Luana; Isabella, Olindo

**DOI**

[10.1002/solr.202100810](https://doi.org/10.1002/solr.202100810)

**Publication date**

2022

**Document Version**

Final published version

**Published in**

Solar RRL

**Citation (APA)**

Han, C., Yang, G., Procel, P., O'Connor, D., Zhao, Y., Gopalakrishnan, A., Zhang, X., Zeman, M., Mazzarella, L., & Isabella, O. (2022). Controllable Simultaneous Bifacial Cu-Plating for High-Efficiency Crystalline Silicon Solar Cells. *Solar RRL*, 6(6), Article 2100810. <https://doi.org/10.1002/solr.202100810>

**Important note**

To cite this publication, please use the final published version (if applicable).  
Please check the document version above.

**Copyright**

Other than for strictly personal use, it is not permitted to download, forward or distribute the text or part of it, without the consent of the author(s) and/or copyright holder(s), unless the work is under an open content license such as Creative Commons.

**Takedown policy**

Please contact us and provide details if you believe this document breaches copyrights.  
We will remove access to the work immediately and investigate your claim.



We provide custom laboratory and pilot equipment to printed electronics research & industry

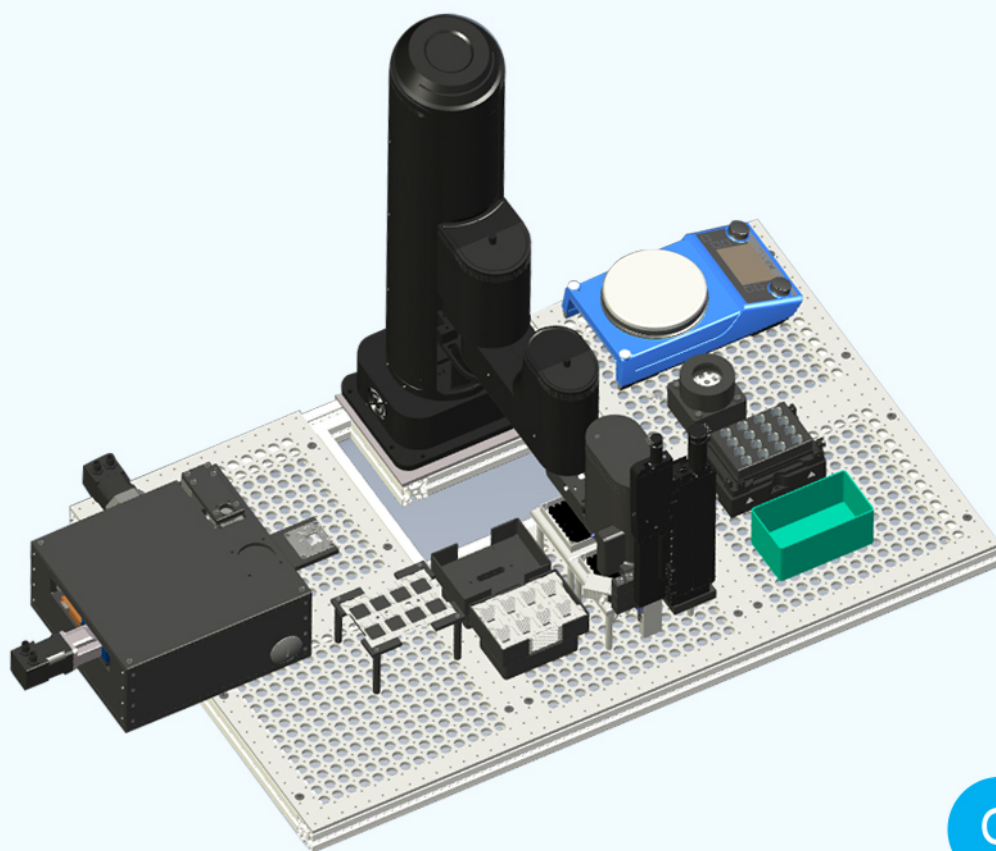
# SpinBot One

*a fully automated, customizable spin-coating robot*

- **Graphical user interface** to control deposition process
- **Automated processing** of 100s of substrates
- 1 substrate per minute using **multiple spincoaters in parallel**
- Full **process control** and reproducibility
- **Database capability** storage of process parameters and measurement results per sample

## Ready for

- **glovebox integration**
- integration of **characterization tools**
- **process integration to full devices** with electronic measurement tools and compatible to evaporation units



[Click to find out more](#)



*Innovative automated scientific solutions*

# Controllable Simultaneous Bifacial Cu-Plating for High-Efficiency Crystalline Silicon Solar Cells

Can Han,\* Guangtao Yang, Paul Procel, Daragh O'Connor, Yifeng Zhao, Anirudh Gopalakrishnan, Xiaodan Zhang, Miro Zeman, Luana Mazzarella, and Olindo Isabella\*

Bifacial (BF) copper-plated crystalline silicon solar cell is an attractive topic to concurrently reduce silver consumption and maintain good device performance. However, it is still challenging to realize a high aspect ratio (AR) of the metal fingers. Herein, a new type of hybrid-shaped Cu finger is electromagnetically fabricated in a BF plating process. Cyclic voltammetry is employed to disclose the electrochemical behaviors of cupric ions in monofacial and simultaneous BF Cu-plating processes, such that the controllability of the plating process could be assessed. The optimal hybrid Cu finger is composed of a rectangular bottom part and a round top part, such that an utmost effective AR value of 1.73 is reached. In BF Cu-plating, two sub-three-electrode electrochemical cells are employed to realize equal metal finger heights on both sides of the wafer. Compared to our low thermal-budget screen-printing metallization, the Cu-plated silicon heterojunction devices show both optical and electrical advantages (based on lab-scale tests). The champion BF Cu-plated device shows a front-side efficiency of 22.1% and a bifaciality factor of 0.99.

## 1. Introduction

Silver (Ag) consumption in the photovoltaic (PV) industry, which takes around 10% of the yearly global Ag production, is becoming a great concern in the PV community.<sup>[1–3]</sup> In 2020, the global solar PV capacity was approximately 135 GW, and an annual production of PV systems of around 3 terawatt (TW) per annum is predicted around 2030,<sup>[1,2,4]</sup> which is tens of times higher than the current capacity. Even if we ignore the evolution in c-Si PV technologies (e.g., silicon heterojunction [SHJ], or industrial Tunnel Oxide Passivated Contact (i-TOPCon) consume more silver than passivated emitter and rear cell (PERC) per wafer), the global silver production cannot satisfy the vast demand in future decades. Thus, it is imperative to reduce Ag usage. To concurrently reduce Ag consumption<sup>[2,4]</sup> and reach high PV device performance,

bifacial (BF) copper (Cu)-plated solar cell has been an attractive topic in recent years.<sup>[5–7]</sup> High efficiency above 24% has been achieved on industrial 6" BF Cu-plated SHJ solar cells.<sup>[6]</sup> Australian startup SunDrive has obtained an efficiency of 25.54% on commercial-sized SHJ solar cell with Ag-free Cu metallization technology (monofacial [MF] or BF solar cell design unknown).<sup>[8]</sup>

To realize a BF plating process, the approach can be realized in a 2-step process, that is, first do plating on one side of the wafer (with the other side protected or biased) and then plate on the other side.<sup>[9–11]</sup> The other way to do BF plating is a 1-step process, that is, do simultaneous plating on both sides of the wafer.<sup>[5–7,12]</sup> The first BF plating attempt in PV devices was electroless plating. Back to the 1990s, Ebong et al.<sup>[13]</sup> at the university of new south wales (UNSW) tried simultaneous electroless chemical nickel (Ni)-/Cu-plating on both sides of the wafer. But they did not get the same deposition rates on n- and p-sides of the wafer.<sup>[14]</sup> In 2017, Tous et al.<sup>[12]</sup> and Russell et al.<sup>[15]</sup> from interuniversity microelectronics centre (IMEC) reported successful BF electroless Ni plating by applying a proprietary selective activation step on silicon surfaces. Since 2010s, the 2-step BF plating with a combination of a light-induced plating and a field-induced plating on two sides of the wafer,<sup>[11,16,17]</sup> as well as the 1-step simultaneous BF electrochemical plating on both sides of the wafer,<sup>[5–7]</sup> have been extensively developed. The institutes (such as Fraunhofer ISE,

C. Han, G. Yang, P. Procel, D. O'Connor, Y. Zhao, A. Gopalakrishnan, M. Zeman, L. Mazzarella, O. Isabella  
Photovoltaic Materials and Devices group  
Delft University of Technology  
2628 CD Delft, The Netherlands  
E-mail: C.Han-1@tudelft.nl; O.Isabella@tudelft.nl

C. Han  
Shenzhen Institute of Wide-bandgap Semiconductors  
Shenzhen 518055, China

P. Procel  
Instituto de Micro y Nanoelectrónica  
Universidad San Francisco de Quito  
Quito 170 901, Ecuador

X. Zhang  
Institute of Photoelectronic Thin Film Devices and Technology  
Nankai University  
Tianjin 300350, China

 The ORCID identification number(s) for the author(s) of this article can be found under <https://doi.org/10.1002/solr.202100810>.

© 2022 The Authors. Solar RRL published by Wiley-VCH GmbH. This is an open access article under the terms of the Creative Commons Attribution-NonCommercial-NoDerivs License, which permits use and distribution in any medium, provided the original work is properly cited, the use is non-commercial and no modifications or adaptations are made.

DOI: 10.1002/solr.202100810

CSEM, UNSW, SIMIT<sup>[5]</sup>, and companies (such as MECO, Sunpreme) are working on the BF Cu-plating development.<sup>[18]</sup> However, despite the devoted efforts, the Cu-plating development is still not ripe enough to compete with traditional screen printing (SP) technology. The market share of Cu-plated solar cells is still conservatively considered,<sup>[19]</sup> which is predicted to about 12% in 2031.<sup>[20]</sup> The factors that hamper the progress of plating technique include processes, equipment, and reliability issues.<sup>[20]</sup> Therefore, research on these aspects is essential to the development of the alternative Cu-plating metallization approach in next decade(s).

Regarding the 1-step simultaneous BF electrochemical plating process, provided the wafer is double-sided coated with a full area thin metal seed layer and fully immersed in the electrolyte solution, the wafer could be basically treated as a conductor in the electroplating process, which may introduce influences in the two electrochemical deposition processes on both sides of the wafer. Assuming one does MF electroplating on one wafer side, with the other side immersed in the solution but unprotected (or unbiased), the other side of the wafer can also be plated. Such a “bifacial” plating may be challenging to control due to the complex uncertainties in the wafer surface condition, electrolyte, and the distribution of electric field.<sup>[21–24]</sup> Therefore, it is imperative to carry out investigation to understand the electrochemical behaviors of the reactive species in the BF electroplating processes and realize them in a controllable way.

In addition, from the finger dimension point of view, a high aspect ratio (AR, i.e., the ratio of height and width) is always desirable to ensure sufficient conductivity and minimize shadow losses at the illuminated side(s) of solar cells.<sup>[19]</sup> In general, there are two basic types of metal finger cross sections in PV devices: (i) rectangle-like shape,<sup>[25]</sup> from self-aligned metal growth in specific contact pattern; (ii) half-circular shape, from free isotropic growth of metal after initial nucleation at specific nucleation point (or hole).<sup>[26]</sup> The latter type is optically preferable because with an encapsulated wavy metal finger joint by half-sphere-shaped metal points, Blakers et al. calculated the effective shading to be below 36%.<sup>[26]</sup> However, plating the half-sphere-shaped metal points at the designed position requires an extremely narrow starting finger width at pointed places.<sup>[26]</sup> This increases the complexity in the control of metal plating process. In addition, such a half-circular shape geometrically sets an intrinsic constant AR value of the finger. To minimize the effective shading loss of the plated Cu finger, pioneers in Atotech<sup>[27]</sup> and Fraunhofer ISE<sup>[28]</sup> have been devoting efforts to change the isotropic growth of Cu to anisotropic feature via electrolyte tuning. Other alternative approaches are also in progress.

In this work, we employ two sub-three-electrode electrochemical cells in simultaneous BF Cu-plating processes. Via cyclic voltammetric (CV) study, we provide an alternative method to monitor whether the simultaneous BF Cu-plating process is well controlled. In addition, to reach a high-effective AR of the metal finger, we fabricate a new type of hybrid-shaped Cu finger whose cross section combines a rectangle-like bottom part and a round top part. Finally, we test the optimal BF plated Cu finger in SHJ solar cells at lab-scale.

## 2. Results and Discussion

### 2.1. Cyclic Voltammetric Study

Figure 1a shows the first two subsequent CV scans in MF deposition process. On the first scan, the forward scanning current starts from a near zero value, and displays a seemingly cathodic deposition peak feature at around  $-0.32$  V. While on the second scan, the cathodic deposition peak features appear at around  $-0.11$  and  $-0.27$  V. This indicates that Cu becomes easier to be plated on the initially grown Cu, rather than the original physical vapor deposition (PVD) Ag-seed layer. This observation agrees with the report from Dobson et al.,<sup>[29]</sup> and could be treated as an overpotential deposition (OPD) of Cu on Ag. The OPD phenomenon could be explained by the lower binding energy of a Cu adatom on Ag than the Cu bulk cohesive energy.<sup>[30,31]</sup> Figure 1b shows the comparative CV scans between MF and BF deposition processes. There are two specific local deposition peak features appearing at different voltages during a forward potential scan, which could correspond to the two-electron transfer steps involved in the reduction of the cupric ions in the solution,<sup>[32,33]</sup> as indicated in the same figure. The redox reactions are provided in Figure 1b. One can see that, with simultaneous control on the two electrochemical cells, the cathodic currents on both sides of the wafer are almost identical. In addition, with respect to the MF deposition, the cathodic current in BF deposition is smaller, and the current peaks shift to lower deposition voltage values. This manifests that although the CV features of the both side scanings in BF process overlap with each other, they are not equal to the case of a single electrochemical cell. This could be related to the fact that the wafer itself is a conductor in the plating bath. The applied potential on one sub-cell on one side of the wafer would unavoidably influence the other conductive side of the wafer, thus somehow interacting with the electrochemical process in the other sub-cell on the other side of the wafer. In other words, the BF Cu deposition rates on both sides of the wafer can be controlled at the same level, but they are not the same as that of MF deposition. It is noteworthy that our CV study only provides qualitative analysis in recognizing the difference in MF and BF deposition processes, since we utilized a diluted electrolyte solution in CV study (due to the upper current limit in our potentiostat tools). Investigations with the real electrolyte concentrations of electroactive species may provide more detailed understanding on how the electrochemical interaction occurs in different electrochemical reactions during MF and BF depositions. In addition, we observed a slight difference in the absolute current density values between the black curves in Figure 1a,b, which could be related to the possible differences in our textured electrode surface, surface contamination, or environmental perturbation during the CV scans.

Figure 1c shows the CV scans on one side of the wafer in BF deposition process, with varied scan rates ( $\nu$ ). The data on the other side of the wafer basically overlaps with the data in Figure 1c, thus is not shown. One can see that, with varied  $\nu$  values, the voltage that corresponds to the peak current ( $i_p$ ) changes. This is a characteristic of the electrochemical irreversibility feature of the Cu electrodeposition process. It means that the electron transfer at the working electrode (WE) is slow compared to mass transport, thus significantly more negative applied potentials than the theoretical redox potential may be required for

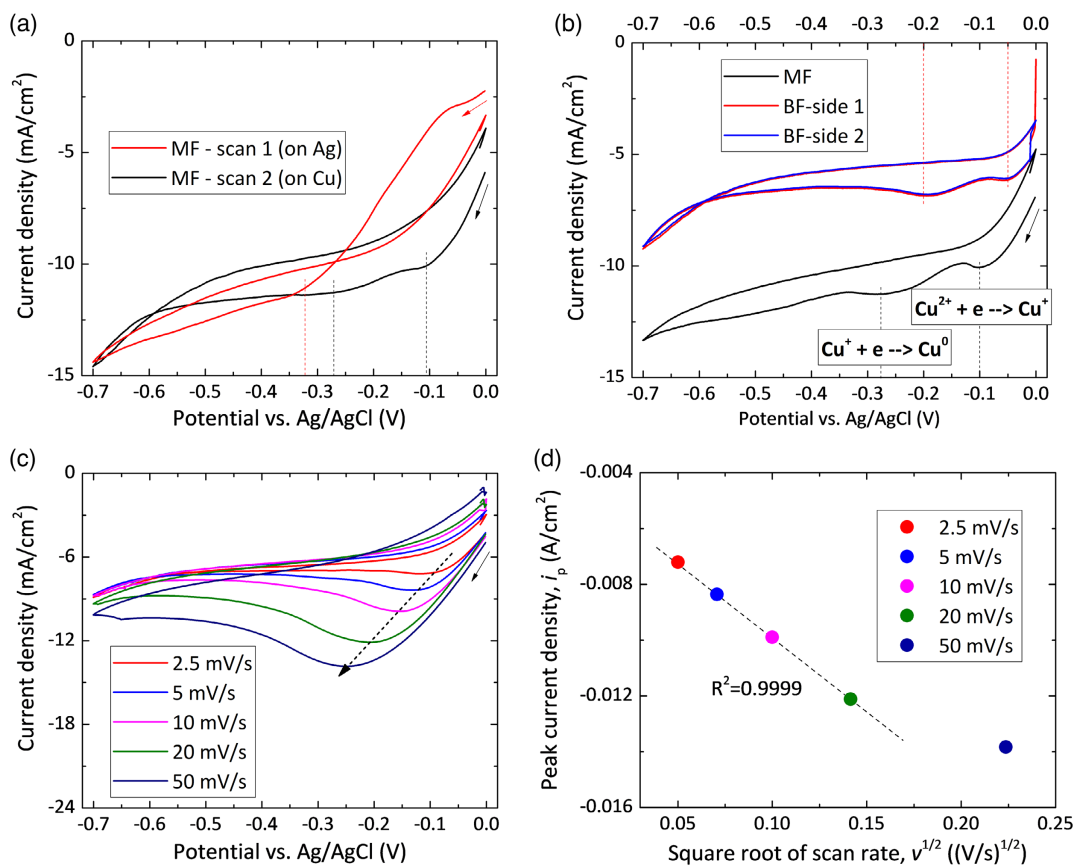


**Figure 1.** a) The first two subsequent cyclic voltammetric (CV) scans in monofacial (MF) deposition process; b) comparative CV scans between MF and bifacial (BF) deposition processes, in which the reaction equations are also involved; c) CV scans with varied scan rates and d) the cathodic peak currents ( $i_p$ ) versus the square root of the scan rate ( $v^{1/2}$ ) in BF deposition.

appreciable current to flow.<sup>[21,34]</sup> Figure 1d depicts the data points of  $i_p$  versus  $v^{1/2}$ , and corresponding linear fitting line. According to the Randles–Sevcik equation for the irreversible electrochemical process,<sup>[35]</sup>  $i_p = -0.496\sqrt{an'}nFAC\sqrt{\frac{nFDv}{RT}}$ , in which  $F$  is the Faraday constant,  $R$  is the universal gas constant,  $T$  is the temperature,  $A$  is the electrode area,  $C$  is the bulk concentration of the solution,  $D$  is the diffusion coefficient of the electroactive species,  $\alpha$  is the transfer coefficient, and  $n'$  is the number of electrons transferred before the rate determining step. For  $v$  increasing from 2.5 to 20  $\text{mV s}^{-1}$ , the relation of  $i_p$  versus  $v^{1/2}$  shows a linear behaviour, indicating that the redox species are freely diffusing in the solution.<sup>[21,36]</sup> The case of 50  $\text{mV s}^{-1}$  shows an obvious deviation from the fitted line of other data points. This might be caused by the fact that the Randles–Sevcik equation is derived assuming the concentration of the electroactive species in the bulk is the same as that at the surface of the electrode. When  $v$  is too high, the assumption may not be valid, and the linear formula does not hold anymore.<sup>[35]</sup> In addition, it is noteworthy that there is some noticeable cathodic deposition feature change between the curves from the same parameter setting, such as between the “BF-side 1” curve in Figure 1b and the “2.5  $\text{mV s}^{-1}$ ” curve in Figure 1c. This is possibly caused by the WE surface condition change or the adsorption of solvent impurities on the counter electrodes (CEs).<sup>[21]</sup> For

comparison purposes, the CV curves of MF deposition process with varied scan rates are provided in Figure S1, Supporting Information. Basically, the MF depositions occur at more negative voltages than that in BF deposition cases, which is in agreement with the observations of Figure 1b. In addition, the MF deposition process also shows an irreversible characteristic. However, we would like to point out that, due to the upper current limitations of our potentiostat tools, we used diluted solution in the CV study, rather than the formal Cu-plating bath (see Experimental Section). The bulk concentration change influences both the absolute redox potential and  $i_p$  values.<sup>[21]</sup> Therefore, the results from Figure 1c,d only provide a tentative understanding of the electrochemical plating processes. Nevertheless, the indications from comparative CV results could be still legitimate, which include the following: (i) the initial Cu growth on Ag-seed layer belongs to OPD; (ii) the simultaneous deposition processes on both sides of the wafer are basically identical in BF deposition, but they differ from MF deposition process; (iii) the BF deposition tends to occur at smaller voltages than MF case, and the cathodic current is smaller than in MF case.

## 2.2. Optimal BF Cu Plating with 2-Step Deposition Approach

We optimized galvanostatic BF Cu-plating process. The current-time condition of  $-0.4 \text{ A}$  (corresponding to approximately

$-20 \text{ mA cm}^{-2}$ ) for 20 min was found to be the best current–time condition to produce  $\approx 30 \mu\text{m}$  finger height (similar as that of our screen-printed Ag). However, the adhesion and uniformity of the finger height over the active area of the solar cell were found to be poor probably due to the reasons coming from (i) geometrical contact design,<sup>[24]</sup> including the height of these plated contacts; (ii) crystallographic coherency at the interface between plated metal and the substrate<sup>[37]</sup>; and (iii) nuclei germination and coalesce control in the metal growth.<sup>[38,39]</sup> As indicated by literature and the CV study results in Figure 1a, we performed two-step depositions. Prior to the optimal galvanostatic “1-step” process ( $-0.4 \text{ A}$ , 20 min), we added either another galvanostatic process ( $-0.2 \text{ A}$ , 2 min) or a potentiostatic process ( $-0.35 \text{ V}$ , 2 min), namely, “2-step(I)” and “2-step(II)”, respectively. **Figure 2a** shows the photo of one solar cell on one side of the wafer, and **Figure 2b** shows a typical finger height distribution along the middle finger as indicated in **Figure 2a**. One can see that, as compared to “1-step” case, the finger height uniformity is significantly improved with both 2-step approaches. In addition, in our adhesion test with a tape, the fingers from “1-step” deposition mode tended to easily detach off the substrate. While for the fingers deposited from “2-step” modes, no detachment was observed. The “2-step” approaches were also reported from the literature,<sup>[38,39]</sup> with the purpose of improving adhesion between Cu and the underlying foreign substrate and forming homogeneous Cu growth. The rationale of the improvement could be attributed to the manipulation of the island nucleation and growth in the electrochemical deposition, which dictates the structure and properties of the plated metal.<sup>[40]</sup> However, we note that even with the “2-step” modes, the uniformity of our Cu finger height is still not ideally controlled, that is, the finger height at the edge part of the solar cell is still  $4\text{--}6 \mu\text{m}$  lower than that of the central region. This could be related to the intrinsic ununiform current distribution between the finger and the adjacent busbar regions in the plating process.<sup>[24]</sup> Further attempts to improve the homogeneity, such as applying a narrower busbar or busbar-free cell design, are under investigation.

Since galvanostatic mode is widely utilized in compact metal electrode electrodepositions, we set the “2-step(I)” as the optimal plating process. The faradaic current efficiency ( $CE_F$ ) is defined

as the ratio of the experimentally obtained amount of material deposited to its theoretical calculation according to Faraday’s equation. It is mathematically expressed as  $CE_F = \frac{mFz}{MIIt}$ ,<sup>[41]</sup> where  $m$  represents the measured mass of elements deposited at the cathode,  $F$  is Faraday’s constant ( $96\,485 \text{ C mol}^{-1}$ ),  $z$  is the valence of the ions,  $M$  is the molar mass of the substance,  $I$  is the applied current, and  $t$  expresses the deposition time. Accordingly, the  $CE_F$  of our BF plating process corresponds to 89.4%. We note that the  $CE_F$  of MF plating process from the same plating parameter setting as in BF plating was determined to be 99.7%, indicating an ideal utilization of the applied current. This is another indication (in addition to **Figure 1b**) that the electrochemical process on one side of the wafer in BF deposition is not equal to single MF deposition. Additionally, the  $CE_F$  of MF plating is much higher than the current efficiency of 30% in our previously reported MF Cu-plating process.<sup>[42]</sup> The  $CE_F$  improvement could be mainly ascribed to the fresh and optimal commercial electrolyte solution use, as well as the modification in circuit connections.

### 2.3. Morphological Manipulation

**Figure 3a–c** shows the morphological manipulation of the plated Cu finger. **Figure 3a** illustrates the cross section of a typical half-sphere metal finger with encapsulant or glass,<sup>[43]</sup> in which A and B fractions could effectively reduce the shadow loss of the finger owing to the downward trajectory of the light path and total reflection at glass–air interface, respectively. While the fraction C could be assumed to be a lambertian emitter, where the incoming light is completely reflected out in each angle.<sup>[43,44]</sup> According to Blakers et al.<sup>[26]</sup> and Woehl et al.,<sup>[43]</sup> when a half-sphere-shaped finger is covered with encapsulant, only a top portion (fraction C) in the half-circular cross section is acting as a shadow area. The geometrical portions of the areas A, B, and C are calculated in **Figure S2**, Supporting Information. **Figure 3b,c** shows the scanning electron microscope (SEM) images of the cross section of two types of hybrid fingers we fabricated. We controlled the finger shape via tuning the contact pattern (mask layer) from lithography procedure. The prototype sketches of **Figure 3b,c** are shown in **Figure S3a,b**, Supporting Information, respectively. Each hybrid

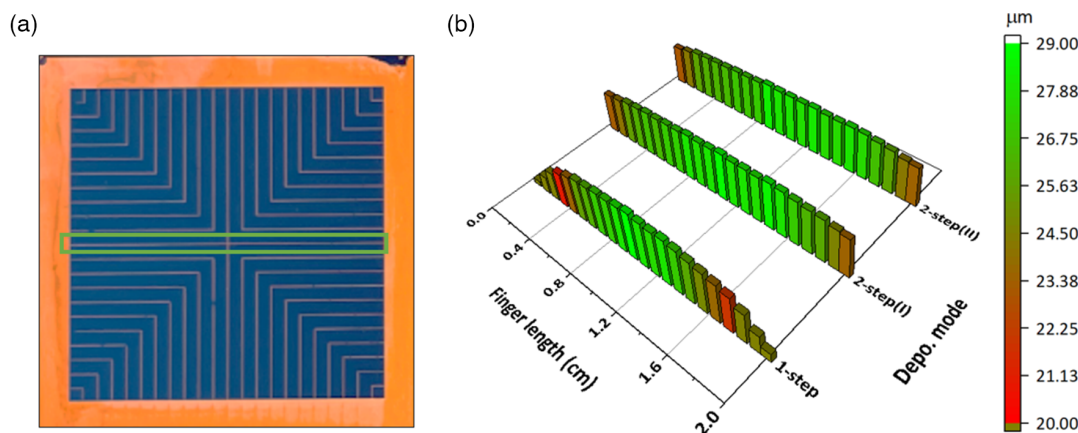


**Figure 2.** a) Image of one solar cell (active area  $2 \times 2 \text{ cm}^2$ ) on one side of the wafer. b) Finger height distribution along the 2 cm long middle finger indicated by the green rectangle in (a) for different deposition modes.

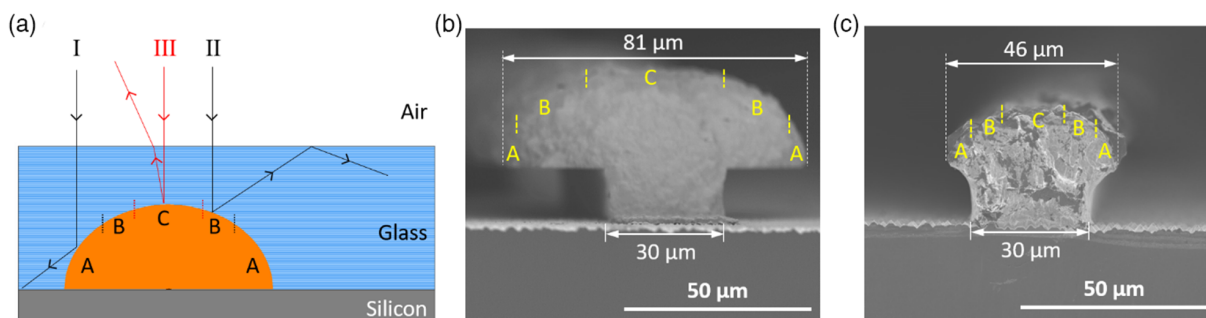


**Figure 3.** a) Schematic cross-sectional view of an encapsulated half-sphere-shaped metal finger, in which A, B, and C indicate areas with different reflection properties. b,c) Scanning electron microscope (SEM) images of the cross section of our hybrid-shaped fingers.

finger consists of a rectangle bottom part and a round top part, such that the novel structure could maintain the favourable optical advantage from half-circular-shaped finger, meanwhile high AR could be potentially achieved.

The effective AR ( $AR_{\text{eff}}$ ) can be introduced to obtain an optical evaluation of our hybrid metal fingers. The expression is as follows

$$AR_{\text{eff}} = \frac{h_{\text{finger}}}{\max(w_{\text{top}}, w_{\text{bot}})} \quad (1)$$

where  $h_{\text{finger}}$  denotes the total height of the metal finger,  $w_{\text{top}}$  and  $w_{\text{bot}}$  are the calculated width of the shadow area C (i.e.,  $w_{\text{top}} = w_{\text{C}}$ ) at the top round part and the measured width of the finger at the bottom rectangular part, respectively. The  $\max(w_{\text{top}}, w_{\text{bot}})$  represents the maximum of the values of  $w_{\text{top}}$  and  $w_{\text{bot}}$ . The  $AR_{\text{eff}}$  describes the ratio of the finger height and the actual shadow area width when covered with encapsulant. The  $AR_{\text{eff}}$  is  $\frac{h_{\text{finger}}}{w_{\text{top}}}$  for single round-shaped finger, and is  $\frac{h_{\text{finger}}}{w_{\text{bot}}}$  for single rectangular-shaped finger. Provided normal incoming light is applied, the refractive index of the glass is 1.5 and the metal surface is ideally smooth and reflective, one can calculate the  $w_{\text{C}}$  to be  $\approx 0.36D$  for the finger in Figure 3a, where  $D$  is the diameter of the half-circle (see Figure S2, Supporting Information). Thus, the  $AR_{\text{eff}}$  of the ideally half-sphere-shaped metal finger can be determined to be  $\approx 1.4$ . For the widely utilized rectangular-shaped metal finger, the  $AR_{\text{eff}}$  is equal to AR, and is generally 0.2–1.<sup>[9,18,25,42,45–47]</sup> For the hybrid fingers as shown in Figure 3b,c, the  $w_{\text{top}}$  values are calculated to be 34.3 and 15.4  $\mu\text{m}$ , respectively. The corresponding measured  $h_{\text{finger}}$  values are 41 and 33  $\mu\text{m}$ , and the  $AR_{\text{eff}}$  values are obtained as 1.2 and 1.1, respectively. Therefore, the  $AR_{\text{eff}}$  values of the hybrid fingers of Figure 3b,c are comparable and fall in-between that of single rectangular-shaped and single half-sphere-shaped fingers.

However, the hybrid Cu finger in Figure 3c is more optically favourable than the one in Figure 3b for three reasons. First, from the finger growth mode point of view, the finger in Figure 3b tends to have a large overall width (81  $\mu\text{m}$ ) and a greater  $w_{\text{top}}$  than  $w_{\text{bot}}$ . The former leads to a large diameter ( $D$ ) value of the geometrical circle, and the latter limits the further improvement of  $AR_{\text{eff}}$ . In contrast, the hybrid finger in Figure 3c could potentially reach

higher  $AR_{\text{eff}}$  values due to its notably lower  $w_{\text{top}}$  than  $w_{\text{bot}}$ . Second, from the device design point of view, with respect to the finger in Figure 3b, the smaller overall finger width (46  $\mu\text{m}$ ) in Figure 3c could allow smaller finger-to-finger distance, that is, denser finger distribution, such that the device could be more tolerant of functional layers with high sheet resistance.<sup>[48]</sup> This can be of special importance for the emerging BF transparent conductive oxide (TCO)-less/free SHJ solar cell topic in recent years.<sup>[49,50]</sup> Third, in reality, the  $w_{\text{top}}$  could be higher than the calculated value, which is more detrimental when using the hybrid finger as shown in Figure 3b. The aforementioned calculation of  $w_{\text{top}}$  is based on the assumption that the metal surface is ideally smooth and reflective. However, the actual plated metal finger can be grown into different microscopic morphologies, depending on the growth kinetics and substrate properties. In the case of Figure 3b, the  $\max(w_{\text{top}}, w_{\text{bot}})$  is determined by  $w_{\text{top}}$ . The widening of  $w_{\text{top}}$  means decreasing  $AR_{\text{eff}}$ , thus is not desirable in the actual device utilization. All in all, with respect to the hybrid finger in Figure 3b, the finger growth mode in Figure 3c could potentially achieve metal finger with higher  $AR_{\text{eff}}$ , resulting in both optical and electrical benefits at device level.

#### 2.4. Plated Cu and Screen-Printed Ag Fingers, and SHJ Devices (Lab-Scale)

Based on the favourable finger growth mode in Figure 3c, we further optimized the plated Cu finger by using a smaller feature of  $w_{\text{bot}}$ , reducing the rectangular bottom part. **Figure 4a,b** shows the SEM and the optical microscope images of our optimized hybrid plated Cu finger, which exhibits an  $AR_{\text{eff}}$  value of 1.73. It is worth noting that this method of making hybrid-shaped metal fingers can also be applied to different (smaller) geometrical sizes. By properly tuning the mask design, a flexible approach to grow various expected metal contacts for high-performance PV devices could be facilitated.

For comparison, the images of our lab-standard low-thermal-budget screen-printed (SP) Ag finger are provided in Figure 4c,d resulting in an  $AR_{\text{eff}}$  value of 0.36. Moreover, from Figure 4c,d, with respect to the SP-Ag case, the Cu fingers have a well-defined shape, and the plated Cu is super-conformal, void-free, and in compact contact with the wafer surface (see insets in Figure 4a,b). This implies a good electrical contact between plated Cu and the underlying Ag(seed)/indium tin oxide

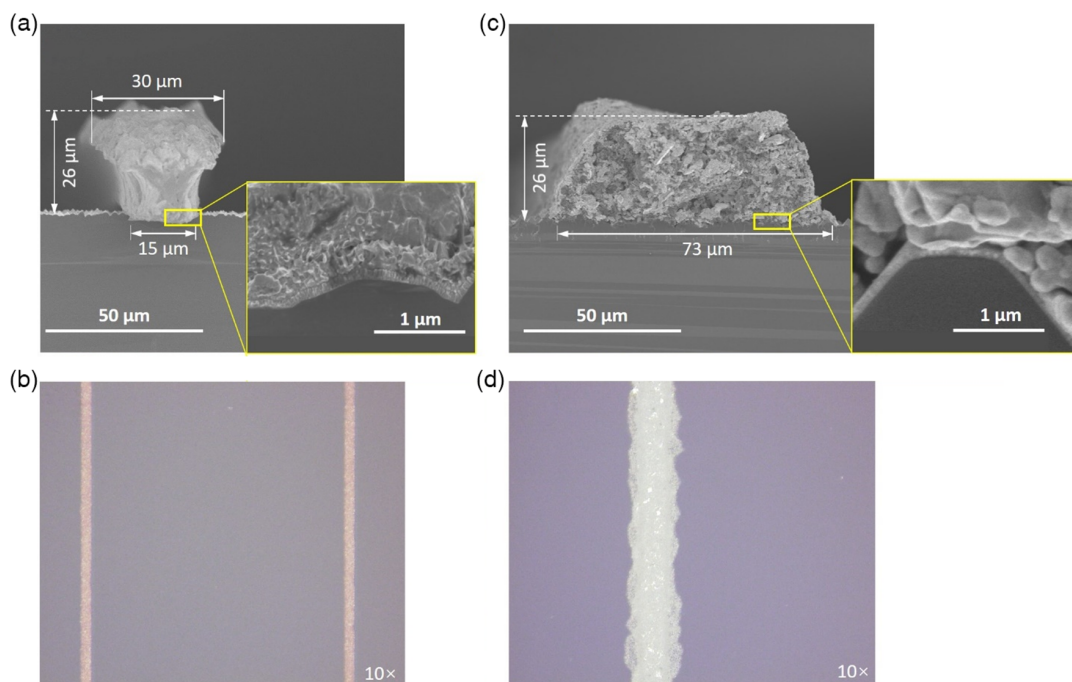


**Figure 4.** a) SEM images and b) optical microscope images of our optimal hybrid Cu finger. c) SEM and d) optical microscope images of the lab-standard screen printing (SP)-Ag finger.

(ITO)/doped silicon film stacks. Additionally, from dedicated contact design with different contact width and 4-point probe measurements, the estimated resistivity of our plated Cu finger is calculated to be  $1.7 \pm 0.1 \mu\Omega \text{ cm}$ , which is comparable to the Cu bulk material. In contrast, the resistivity of our lab-scale standard SP-Ag finger is  $10.0 \pm 5.0 \mu\Omega \text{ cm}$ . There are two aspects to be noted. First, as mentioned in Experimental Section, the raw finger resistivity values are calculated from the measured finger resistance and related geometrical dimensions, and the latter could intrinsically bring uncertainties due to the nonstandard/nonuniform geometrical shapes of the fingers. Second, the resistivity value of our screen-printed Ag finger is limited by issues such as setup, paste, and curing condition in the laboratory, and cannot be representative of state-of-the-art screen-printed Ag finger as obtained in an optimized industrial environment.

**Table 1** shows the comparative BF SHJ solar cell results with plated Cu and SP-Ag metallization approaches, from front-side (*i/n*) illumination. The Cu-plated cell outperforms the SP cell both optically and electrically. Specifically, the cell with SP-Ag showed lower open-circuit voltage ( $V_{OC}$ ), with respect to the Cu-plated cell. This could be partially caused by the Ag

penetration into wafer bulk, which induces more recombination centres at the metal and silicon interfaces. Supportive information could be found in Figure S4, Supporting Information, in which one can clearly see the damaged pyramid structures by metal penetration of SP-Ag into the silicon substrate. In addition, we note that the implied  $V_{OC}$  ( $i - V_{OC}$ ) of both SHJ cell precursors was  $\approx 740 \text{ mV}$  before metallization procedure. Surprisingly, the difference between  $i - V_{OC}$  and  $V_{OC}$  was observed to be  $>20 \text{ mV}$ , even for the Cu-plated cells. This manifests that the quasi-Fermi level splitting of majority and minority carriers in the absorber was not effectively transferred to the external voltage.<sup>[51–53]</sup> Detailed diagnosis is under investigation.

Regarding the optical response, the higher short-circuit current density ( $J_{SC}$ ) in Cu-plated solar cells could be explained by its lower metal coverage of 1.6% than the 4.4% of the SP-Ag solar cells. In addition, it is noteworthy that the cells were not encapsulated, thus the measured  $J_{SC}$  is somehow compensated by counting both the fractions B and C as shadow areas, rather than only counting the fraction C as shadow portion in the top finger part (see discussion related to Figure 3a). The finger shape has been reported to play an important role in the

**Table 1.** Solar cell parameters of  $4 \text{ cm}^2$  silicon heterojunction (SHJ) devices with plated Cu and screen printing (SP)-Ag metallization approaches. The cell precursors were fabricated from one batch. The designed metal coverage values are 1.6% and 4.4%, respectively. The reported values are the average based on three cells illuminated from front side (*i/n*). The standard deviation is calculated for each external parameter.

	Open-circuit voltage [ $V_{OC}$ , mV]	Short-circuit current density [ $J_{SC}$ , $\text{mA cm}^{-2}$ ]	Pseudo fill factor [ $pFF$ , %]	Fill factor [ $FF$ , %]	Efficiency [ $\eta$ , %]
Plated Cu	$716 \pm 1.5$	$38.07 \pm 0.04$	$85.10 \pm 0.36$	$80.76 \pm 0.04$	$22.02 \pm 0.06$
SP-Ag	$710 \pm 3.5$	$37.24 \pm 0.02$	$84.07 \pm 0.12$	$76.11 \pm 0.07$	$20.12 \pm 0.10$

optical properties in the module.<sup>[43,44,54,55]</sup> We believe that the optical advantage of the Cu-plated cell over the screen-printed cell is potentially higher when measured with encapsulated cells.<sup>[43,54]</sup> As for the fill factor (*FF*) of the cells, with respect to the SP cells, the Cu-plated SHJ cell shows a significant average *FF* improvement by 4.65%<sub>abs.</sub> It has been theoretically and experimentally proven that the c-Si absorber itself could provide sufficient lateral electron transport toward the metal electrodes.<sup>[50,56]</sup> For the p-side, we calculated the diffusion length of the holes to be 1080  $\mu\text{m}$ . This value is bigger than the finger gap of 915  $\mu\text{m}$  in plated Cu grid, but smaller than the finger gap of 1740  $\mu\text{m}$  in printed Ag grid. Therefore, the low *FF* in the screen-printed cell should be mainly caused by the large finger gap on the p-side of the cell. Additional factors, such as finger resistance, the contact resistivity at the layer interfaces, and the selectivity of the functional layers in the cell precursors, remain to be investigated. The measured pseudo *FF* (*pFF*) values are also included in Table 1, based on which the series resistance ( $R_{s,\text{Suns}V_{oc}}$ ) values were calculated to be  $0.93 \pm 0.02$  and  $1.71 \pm 0.02 \Omega \text{cm}^2$ , for Cu-plated solar cell and SP counterpart, respectively. The overall power conversion efficiency shows an average improvement of 1.9%<sub>abs.</sub> **Figure 5** shows the corresponding comparative *J-V* curves and cell parameters of our champion devices, from n-side illumination. One can clearly see the optical and electrical advantages in Cu-plated cell over the screen-printed counterpart. The champion BF Cu-plated SHJ device shows a power conversion efficiency of 22.10% from front-side (*i/n*) illumination. Measuring from p-side illumination, the bifaciality factor was calculated to be 0.99. In addition, it may be important to note that the data in Table 1 and Figure 4 are from this laboratory case study. In other words, one cannot treat the comparative data as evidence of technical outperformance of Cu-plating technique over screen-printing technique. In addition, the issues we have in our lab-scale, standard, and screen-printed solar cells may not exist at an industrial level. Thus, the purpose of the earlier

analysis only lies in gaining insights about the cause of the observed difference in our solar cell performance.

### 3. Conclusions

In summary, via CV approach, we studied the electrochemical behaviors on both sides of the wafer in the one-step simultaneous Cu-plating process, based on which the evaluation on the double-side plating control can be made. The results show that the initial Cu growth on Ag-seed layer is an OPD. With a 2-step deposition approach, we improved finger adhesion and achieved relatively uniformly distributed Cu fingers. With appropriate morphological manipulation on the plated Cu finger, we fabricated a new type of hybrid-shaped Cu finger, which consists of a rectangular bottom part and a round top part with an utmost  $AR_{\text{eff}}$  value of 1.73. Finally, with respect to our lab-scale, standard, and low-temperature screen-printed SHJ solar cells, the Cu-plated devices showed both optical and electrical advantages. The champion BF Cu-plated device shows a power conversion efficiency of 22.1% from front-side (*i/n*) illumination, and a bifaciality factor of 0.99.

### 4. Experimental Section

A basic Cu-plating process consisted of (i) full area 100 nm thick Ag-seed layer growth by PVD deposition and contact pattern by photolithography on both sides of the wafer. AZ EC13027 photoresist and tetramethylammonium hydroxide (TMAH)-based MF322 developer were utilized in standard micro-electromechanical systems (MEMS) lithography processes. A constant resistance value of 0.1  $\Omega$  was ensured at the Ag-seed layer surface after PVD and before Cu plating (measured between randomly distributed points in the contact area); (ii) CV scanning or electroplating of Cu; (iii) removal of the photoresist and Ag-seed layer from the un-plated area. More details about the process sequence could be found elsewhere.<sup>[42]</sup> A dual-functional sample holder, which could contact the seed layer on each side of the wafer individually with 2 separated potentiostat tools, was designed for satisfying both MF and BF electroplating purposes. To ensure a homogenous current distribution in the electrochemical process, a surrounding electric contact was utilized by sandwiching the wafer between two metal rings, whose outer circles matched the shape of the wafer. It was worth noting that a parasitic Cu plating on the wafer edge occurred, no matter whether the full area PVD Ag-seed layer was deposited with or without the wafer edge exclusion. The wafer edge deposition was also reported by Hatt et al.<sup>[57]</sup> and Grubel et al.<sup>[10]</sup> In addition, we assumed that the wafer itself and its surrounding functional layers did not participate in the Cu-plating process, for the following two reasons: (i) in an electrochemical cell, the applied charges from the potentiostat were mainly consumed by electrochemical reactions at the Ag-seed layer surface; (ii) the energy barriers between wafer and other functional layers (such as thin-film silicon layers and transparent conductive oxide layer) blocked the residual electron flow from the Ag-seed layer to the functional layers underneath.

**Figure 6a** depicts the basic experimental configuration of our Cu-plating processes, in which two sets of standard 3-electrode cells were utilized with Ag/AgCl reference electrodes (RE). All voltages were reported with respect to the Ag/AgCl RE. Regarding the sample geometry in CV study, we used  $1 \times 1 \text{ cm}$  square full area contact design in the middle of the wafer substrate. In both MF and BF experiments, the wafer was double-side coated with photoresist. In MF case, only one side was opened with the aforementioned square contact design; in BF case, both sides of the wafer were opened with the contact design. Two independent Metrohm Autolab potentiostat tools, PGSTAT101 and PGSTAT204, were utilized to separately control the two electrochemical cells on both sides of

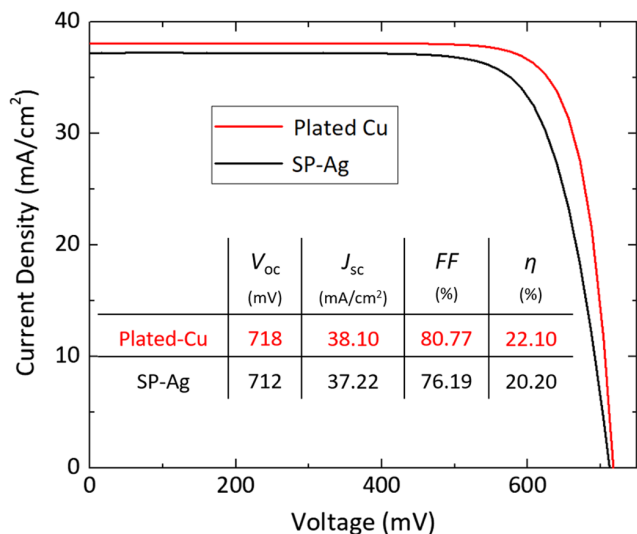


**Figure 5.** Champion BF silicon heterojunction (SHJ) solar cell results with plated Cu and SP-Ag metallization approaches, illuminated from front side (*i/n*). The cell area is  $4 \text{ cm}^2$ , and the designed metal coverage values are 1.6% and 4.4%, respectively.

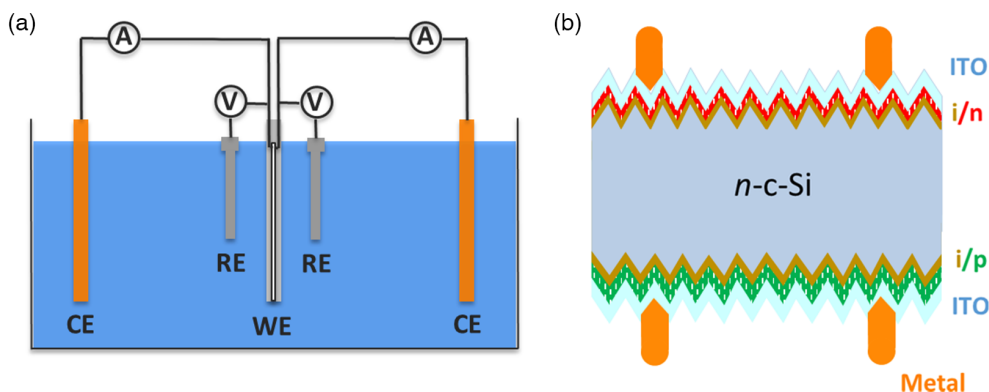


**Figure 6.** a) Schematic experimental configuration of our Cu-plating processes, in which the WE, CE, and RE represent working electrode, counter electrode, and reference electrode, respectively; and b) the SHJ solar cell structure of our photovoltaic (PV) devices.

the wafer. The BF plating by utilizing two potentiostat tools were also reported in literature.<sup>[58]</sup> The WEs were the two sides of the 100 nm thick silver-coated pyramidally textured 4 inch wafer, at which the electrolysis of interest took place within the contact region patterned via photolithography. We carried out the CV study and plating processes at room temperature under quiescent conditions to eliminate any forced convection in the electrolyte solution. However, prior to each experimental batch, the electrolyte solution was stirred for 10 min to form a uniform solution; during one experimental batch, the stirring was done for 2 min in the interval for loading a fresh sample substrate.

For MF CV scans, the back side of the wafer was fully protected with photoresist. The CEs were graphite sheets for CV scan and were sacrificing copper sheets for Cu electroplating process. The dimensions of the CEs were  $10\text{ cm} \times 10\text{ cm} \times \approx 1\text{ mm}$ . Electrodeposition was carried out from an aqueous solution composed of an Intervia 8502 starter solution ( $50\text{ g L}^{-1}\text{ Cu}^{2+}$ ,  $100\text{ g L}^{-1}\text{ H}_2\text{SO}_4$ ,  $50\text{ ppm Cl}^-$ ) and 9000E leveller ( $3\text{ mL L}^{-1}$ ). The pH of the solution was lower than 1. In CV study, due to an upper current limitations of our potentiostat tools, we used 40-fold diluted solution. Although the concentration difference influenced the redox potential of the cupric ions in the solution,<sup>[21,34]</sup> it was still meaningful to use the preliminary CV results from diluted solution to understand the initial electrochemical behaviours of the species, and to qualitatively study the comparative electrochemical behaviours of the redox species in MF and BF deposition processes. In addition, due to the use of a commercial solution, blank solution scan was omitted in our CV investigation. The CV scan started at 0V, then progressed toward the cathodic direction to  $-0.7\text{ V}$ , and finally back to 0V. The scan rate controlled how fast the applied potential was scanned, and was kept at  $2.5\text{ mV s}^{-1}$  unless otherwise specified. Before collecting the data with varied scan rates, we performed several CV scans to exclude the influence of the Ag-seed layer and possible contaminant at the working electrode surface. This was done until two consecutive scans overlapped. To minimize the influence from the resistive losses in the electrical connection in both 3-electrochemical cells, the external resistance in addition to the solution in each cell was controlled to stay below  $0.5\ \Omega$ . The electrode distances of the two sub-cells were kept equal in BF deposition processes, which was approximately  $7.85\text{ cm}$ . The electrode distance in MF Cu-plating utilized the same electrode distance as in BF case. After each deposition, the samples were rinsed with deionized water and dried in air.

Four inch float zone (FZ),  $280\ \mu\text{m}$  thick, and n-type flat (100) oriented wafers ( $1\text{--}5\ \Omega\text{ cm}$ ) were textured with randomly distributed pyramids in a heated solution composed of 5% TMAH and 2.4% ALKA-TEX 8 additive from GP-Solar-GmbH. Figure 6b displays the SHJ solar cell structure of our PV devices. For the device fabrication, after the aforementioned double-side texturization of the wafers, we subsequently cleaned them in two baths of  $\text{HNO}_3$  99% (RT, 10 min) and  $\text{HNO}_3$  69.5% ( $110\text{ }^\circ\text{C}$ , 10 min). Wafers were dipped in 0.55% HF for 4 min prior to the plasma-enhanced chemical vapour deposition (PECVD) step. In this step, the SHJ cell

precursors with front 10 nm thick *i/n* stack and rear 26 nm thick *i/p* stack thin-film silicon layers were prepared. Nominal 75 nm thick ITO films were sputtered on both sides of the wafers. Hard masks were utilized in sputtering step to pattern the cell areas. After sputtering, the wafers went through either the Cu-plating process as described earlier, or a lab-standard low-temperature SP process. The cell area was defined by photolithography or SP screen as  $4\text{ cm}^2$ . For each type of the solar cell, we applied the same metal design on both sides of the wafer. The solar cell images are shown in Figure S5, Supporting Information. For the Cu-plated solar cells, the finger pitch was  $915\ \mu\text{m}$  on both sides of the wafer; while for the screen-printed solar cells, the finger pitch was  $1740\ \mu\text{m}$  on both sides of the wafer. The growth of Cu used the optimal “2-step” electrochemical deposition, which will be introduced in Section 3. In the BF SP case, an optimal curing condition of  $170\text{ }^\circ\text{C}$  for 30 min was utilized to make the metal contact. Specifically, we first performed the SP on the n-side of the wafer, dried the paste on the wafer in an oven at  $170\text{ }^\circ\text{C}$  for 5 min, then carried out the SP on the p-side of the wafer, and did the curing at  $170\text{ }^\circ\text{C}$  for 30 min.

**Finger Characterizations:** The finger height was measured with a Dektak 150 step-profiler. Morphological images of the metal fingers and wafer surfaces were detected with a field-emission SEM (FE-SEM) via Hitachi Regulus 8230, and a low-resolution SEM system from JEOL Ltd., respectively. The optical microscope images of the metal fingers were characterized by a confocal laser microscope (Keyence VK-X250). The resistivity of the metal fingers was obtained from 4-point probe measurements via the electric stage as we used for current-voltage (*I*–*V*) measurements of solar cells. Via a Kelvin connection, the cable resistance in the circuit loop of the measurement setup was excluded. The reported finger resistivity ( $\rho$ ) data were calculated from measured finger resistance (*R*) values via  $\rho = R \cdot S/l$ , where *S* represents the cross-section area of the finger, and *l* denotes the finger length, which was kept at a constant value of 1 cm. Finger samples with different contact width values were utilized ( $15\text{--}50\ \mu\text{m}$  for plated copper finger, and  $50\text{--}100\ \mu\text{m}$  for screen-printed silver finger). In addition, for the plated Cu finger, we performed the tape test to evaluate the finger adhesion.<sup>[42]</sup> It consists of placing a tape on the wafer and then pulling it. If the metal is attached to the tape, the test is considered failed, and the adhesion is considered poor; in contrast, if the test is passed, the adhesion is considered good.

**BF Solar Cell Measurements:** The *J*–*V* characteristics of our  $4\text{ cm}^2$  SHJ devices were measured using an AAA class Wacom WXS-90S-L2 under standard test conditions (STC). A sample stage for BF cell measurement was fabricated in-house for our BF solar cell measurements. In this stage, a special substrate was utilized, showing a reflectance below 3.5% along the wavelength range of  $700\text{--}1200\text{ nm}$ . The reflectance and transmittance curves of the mentioned substrate is provided as Figure S6, Supporting Information. By directly mounting the wafer on the substrate in the *J*–*V* measurements, the rear-side illumination, when measuring the front side of the wafer, could be effectively controlled below  $3\text{ W m}^{-2}$ .<sup>[59]</sup> The *J*–*V* data

were obtained on both sides of the SHJ devices separately. Subsequently, the bifaciality factor,  $\varphi$ , was determined as the minimum of the ratios of the rear and front short-circuit current and maximum power, that is,  $\varphi = \min(I_{sc, rear}/I_{sc, front}, P_{max, rear}/P_{max, front})$ .<sup>[59]</sup> In addition, SunsVoc measurements were performed on our complete BF solar cells via a Sinton Suns-Voc-150 Illumination-Voltage Tester. Note that in SunsVoc measurements, the rear-side reflection from the brass chuck was not excluded.

## Supporting Information

Supporting Information is available from the Wiley Online Library or from the author.

## Acknowledgements

The work has been partially supported by the Science and Technology Program of Guangdong Province (no. 2019B090918006). The authors specially thank Jeroen Lybaert and Martijn Van der Plas in Metrohm for the helpful discussions in fixing the equipment issues for BF Cu-plating process. The authors thank Gregory Pandraud from PVMD group, Robert Verhoeven, Loek Steenweg, and Silvana Milosavljevic from Else Kooi Laboratory at TU Delft for their help in choosing proper plating bath solution and wafer dicing; Dr. Gianluca Limodio in PVMD group for providing the basic Cu-plating flowchart; Martijn Tijssen, Stefaan Heirman, and Remko Koornneef from PVMD group for their technical support.

## Conflict of Interest

The authors declare no conflict of interest.

## Data Availability Statement

The data that supports the findings of this study are available in the supplementary material of this article.

## Keywords

bifacial silicon heterojunction solar cells, Cu-plating, finger shapes, simultaneous electroplating

Received: October 1, 2021

Revised: February 7, 2022

Published online:

- [1] Y. Zhang, M. Kim, L. Wang, P. Verlinden, B. Hallam, *Energy Environ. Sci.* **2021**, *14*, 5587.
- [2] P. Verlinden, *J. Renewable Sustainable Energy* **2020**, *12*, 053505.
- [3] J. C. Goldschmidt, L. Wagner, R. Pietzcker, L. Friedrich, *Energy Environ. Sci.* **2021**, *14*, 5147.
- [4] N. M. Haegel, H. Atwater, T. Barnes, C. Breyer, A. Burrell, Y.-M. Chiang, S. De Wolf, B. Dimmler, D. Feldman, S. Glunz, *Science* **2019**, *364*, 836.
- [5] J. Yu, J. Bian, Y. Liu, F. Meng, Z. Liu, *Sol. Energy* **2017**, *146*, 44.
- [6] A. Lachowicz, J. Geissbühler, A. Faes, J. Champlaud, F. Debrot, E. Kobayashi, J. Horzel, C. Ballif, M. Despeisse, in *33rd EU PVSEC*, Amsterdam, the Netherlands **2017**.
- [7] T. Hatt, J. Bartsch, S. Kluska, M. Glatthaar, *AIP Conf. Proc.* **2019**, *2147*, 040005.

- [8] Sundrive, *Australian startup sets 25.54% efficiency record for silicon cell*, **2021**, <https://www.pv-magazine.com/2021/09/10/australian-startup-sets-25-54-efficiency-record-for-silicon-cell/> (accessed: September 2021)
- [9] Z. Li, P.-C. Hsiao, W. Zhang, R. Chen, Y. Yao, P. Papet, A. Lennon, *Energy Procedia* **2015**, *67*, 76.
- [10] B. Grübel, G. Cimiotti, C. Schmiga, V. Arya, B. Steinhauser, N. Bay, M. Passig, D. Brunner, M. Glatthaar, S. Kluska, *IEEE J. Photovoltaics* **2021**, *11*, 584.
- [11] X. Wang, V. Allen, V. Vais, Y. Zhao, B. Tjahjono, Y. Yao, S. Wenham, A. Lennon, *Sol. Energy Mater. Sol. Cells* **2014**, *131*, 37.
- [12] L. Tous, R. Russell, E. Cornagliotti, A. Uruena, P. Choulat, M. Haslinger, J. John, F. Duerinckx, J. Szlufcik, *Energy Procedia* **2017**, *124*, 922.
- [13] A. Ebong, M. Taouk, S. Wenham, *Sol. Energy Mater. Sol. Cells* **1994**, *31*, 499.
- [14] A. U. Ebong, *PhD Thesis*, University of New South Wales **1994**.
- [15] R. Russell, L. Tous, E. Carnagliotti, D. Hendrickx, F. Duerinckx, J. Szlufcik, in *33rd EU PVSEC*, Amsterdam, the Netherlands **2017**, p. 212.
- [16] B. Grübel, G. Cimiotti, C. Schmiga, S. Schellinger, B. Steinhauser, A. A. Brand, M. Kamp, M. Sieber, D. Brunner, S. Fox, S. Kluska, *Prog. Photovoltaics: Res. Appl.* in press, **2021**.
- [17] J. Bartsch, M. Kamp, D. Hartleb, C. Wittich, A. Mondon, B. Steinhauser, F. Feldmann, A. Richter, J. Benick, M. Glatthaar, M. Hermle, S. W. Glunz, *Energy Procedia* **2014**, *55*, 400.
- [18] S. Kluska, T. Hatt, B. Grübel, G. Cimiotti, C. Schmiga, V. Arya, B. Steinhauser, F. Feldmann, J. Bartsch, B. Goraya, S. Nold, A. Brand, J. Nekarda, M. Glatthaar, S.W. Glunz, *Photovoltaics International* **2020**, *44*.
- [19] G. Beaucarne, L. Tous, J. Lossen, G. Schubert, in *Proc. of the 9th Workshop on Metallization and Interconnection for Crystalline Silicon Solar Cells*, **2021**, p. 020001.
- [20] VDMA, *Inter. Technology Roadmap for Photovoltaic (ITRPV) 12 edition*, **2021**, p. 17.
- [21] N. Elgrishi, K. J. Rountree, B. D. McCarthy, E. S. Rountree, T. T. Eisenhart, J. L. Dempsey, *J. Chem. Educ.* **2017**, *95*, 197.
- [22] S. Y. Tan, V. Y. Y. Chia, K. Hölttä-Otto, F. Anariba, *J. Chem. Educ.* **2020**, *97*, 2238.
- [23] K. Popov, B. Grgur, S. S. Djokić, *Fundamental Aspects of Electrometallurgy*, Springer, Berlin **2007**, pp. 101–142.
- [24] J. O. Dukovic, *J. Electrochem. Sci. Eng.* **1993**, *3*, 117.
- [25] A. Khanna, K.-U. Ritzau, M. Kamp, A. Filipovic, C. Schmiga, M. Glatthaar, A. G. Aberle, T. Mueller, *Appl. Surf. Science* **2015**, *349*, 880.
- [26] A. W. Blakers, *J. Appl. Phys.* **1992**, *71*, 5237.
- [27] S. Kluska, B. Grübel, G. Cimiotti, C. Schmiga, H. Berg, A. Beinert, I. Kubitzka, P. Müller, T. Voss, *EPJ Photovoltaics*, **2021**, *12*, 10.
- [28] T. Hatt, in *Metallization & Interconnection Workshop*, **2021**.
- [29] K. D. Dobson, Z. Sun, U. Nsofor, U. Das, A. Sinha, M. Gupta, S. S. Hegedus, in *2019 IEEE 46th Photovoltaic Specialists Conf. (PVSC)*, IEEE, Piscataway, NJ **2019**, pp. 1112–1119.
- [30] M. Del Pópolo, E. Leiva, *J. Electroanal. Chem.* **1997**, *440*, 271.
- [31] C. Sánchez, E. Leiva, *J. Electroanal. Chem.* **1998**, *458*, 183.
- [32] M.-E. Wagner, R. Valenzuela, T. Vargas, M. Colet-Lagrange, A. Allanore, *J. Electrochem. Soc.* **2015**, *163*, D17.
- [33] A. Milchev, T. Zapryanova, *Electrochim. Acta* **2006**, *51*, 4916.
- [34] G. Zangari, *Coatings* **2015**, *5*, 195.
- [35] A. García-Miranda Ferrari, C. W. Foster, P. J. Kelly, D. A. Brownson, C. E. Banks, *Biosensors* **2018**, *8*, 53.
- [36] L. Sanz, J. Palma, E. García-Quismondo, M. Anderson, *J. Power Sources* **2013**, *224*, 278.
- [37] N. Okamoto, F. Wang, T. Watanabe, *Mater. Trans.* **2004**, *45*, 3330.

- [38] Y. H. Kwon, S. K. Kim, S.-W. Kim, H. K. Cho, *J. Electrochem. Soc.* **2014**, 161, D447.
- [39] F. Goncalves de Cerqueira Lima, U. Mescheder, H. Leiste, C. Müller, *Surf. Coat. Technol.* **2019**, 375, 554.
- [40] L. Guo, G. Oskam, A. Radisic, P. M. Hoffmann, P. C. Searson, *J. Phys. D: Appl. Phys.* **2011**, 44, 443001.
- [41] M. S. Al Farisi, S. Hertel, M. Wiemer, T. Otto, *Micromachines* **2018**, 9, 589.
- [42] G. Limodio, Y. D. Groot, G. V. Kuler, L. Mazzarella, Y. Zhao, P. Procel, G. Yang, O. Isabella, M. Zeman, *IEEE J. Photovoltaics* **2020**, 10, 372.
- [43] R. Woehl, M. Hörteis, S. W. Glunz, *Adv. OptoElectron.* **2008**, 2008, 1.
- [44] O. Schultz-Wittmann, D. De Ceuster, A. Turner, D. Crafts, R. Ong, D. Suwito, L. Pavani, B. Eggleston, in *27th EU PVSEC Frankfurt, Germany* **2012**, p. 596.
- [45] M. Hwang, S. Kim, K. Lee, I. Moon, J. Lim, J. Lee, D. Kyeong, W. Lee, E. Cho, in *25th EU PVSEC Valencia, Spain* **2010**, p. 1792.
- [46] A. Ebong, N. Chen, in *High Capacity Optical Networks and Emerging/Enabling Technologies*, Istanbul, Turkey **2012**, p. 102.
- [47] Y.-H. Chang, W.-M. Su, P.-S. Huang, L.-W. Cheng, in *2013 IEEE 39th PVSC*, IEEE, Piscataway, NJ **2013**, p. 2176.
- [48] A. Aguilar, S. Y. Herasimenka, J. Karas, H. Jain, J. Lee, K. Munoz, L. Michaelson, T. Tyson, W. J. Dauksher, S. Bowden, in *2016 IEEE 43rd Photovoltaic Specialists Conf. (PVSC)*, IEEE, Piscataway, NJ **2016**, p. 1972.
- [49] C. Han, R. Santbergen, M. van Deuffelen, P. Procel Moya, Y. Zhao, G. Yang, X. Zhang, M. Zeman, L. Mazzarella, O. Isabella, unpublished, **2021**.
- [50] S. Li, M. Pomaska, A. Lambertz, W. Duan, K. Bittkau, D. Qiu, Z. Yao, M. Luysberg, P. Steuter, M. Köhler, K. Qiu, R. Hong, H. Shen, F. Finger, T. Kirchartz, U. Rau, K. Ding, *Joule* **2021**, 5, 1535.
- [51] M. Hermle, F. Feldmann, M. Bivour, J. C. Goldschmidt, S. W. Glunz, *Appl. Phys. Rev.*, **2020**, 7, 021305.
- [52] M. Bivour, M. Reusch, F. Feldmann, M. Hermle, S. Glunz, in *Proc. 24th Workshop Crystalline Silicon Sol. Cells Modules, Mater. Processes*, **2014**, p. 1.
- [53] F. Haase, S. Schäfer, C. Klamt, F. Kiefer, J. Krügener, R. Brendel, R. Peibst, *IEEE J. Photovoltaics* **2018**, 8, 23.
- [54] Y. S. Khoo, F. Lu, T. M. Walsh, A. G. Aberle, in *27th EU PVSEC, Frankfurt, Germany* **2016**.
- [55] M. Nicolai, M. Zanucoli, P. Magnone, M. Gializzo, D. Tonini, M. Bertazzo, E. Sangiorgi, C. Fiegna, *Energy Procedia* **2015**, 77, 129.
- [56] J. Haschke, G. Christmann, C. Messmer, M. Bivour, M. Boccard, C. Ballif, *J. Appl. Phys.* **2020**, 127, 114501.
- [57] T. Hatt, V. P. Mehta, J. Bartsch, S. Kluska, M. Jahn, D. Borchert, M. Glatthaar, *AIP Conf. Proc.* **2018**, 1999, 040009.
- [58] J. Yu, L. Zhang, T. Chen, J. Bian, J. Shi, F. Meng, Y. Huang, Z. Liu, *Sol. RRL* **2019**, 3, 1800261.
- [59] T. S. Liang, M. Pravettoni, J. P. Singh, Y. S. Khoo, *Eng. Res. Express* **2020**, 2, 015048.